

See discussions, stats, and author profiles for this publication at: <https://www.researchgate.net/publication/231653281>

# Synthesis of Flower-Like NiO and Effects of Morphology on Its Catalytic Properties

ARTICLE *in* THE JOURNAL OF PHYSICAL CHEMISTRY C · AUGUST 2009

Impact Factor: 4.77 · DOI: 10.1021/jp904186k

---

CITATIONS

110

---

READS

30

7 AUTHORS, INCLUDING:



Yu-Wen Chen

Taiwan Institute of Chemical Engineers, Ta...

168 PUBLICATIONS 3,304 CITATIONS

SEE PROFILE

## Synthesis of Flower-Like NiO and Effects of Morphology on Its Catalytic Properties

Bin Zhao,<sup>†</sup> Xiao-Kang Ke,<sup>‡</sup> Jian-Hua Bao,<sup>‡</sup> Chun-Ling Wang,<sup>†</sup> Lin Dong,<sup>†</sup> Yu-Wen Chen,<sup>\*,§</sup> and Hui-Lan Chen<sup>\*,‡</sup>

Key Laboratory of Mesoscopic Chemistry of MOE, School of Chemistry and Chemical Engineering, Nanjing University, Nanjing 210093, P. R. China, Coordination Chemistry Institute, The State Key Laboratory of Coordination Chemistry, Nanjing University, 210093 Nanjing, P. R. China, and Department of Chemical and Materials Engineering, National Central University, Chung-Li 320, Taiwan

Received: May 5, 2009; Revised Manuscript Received: June 8, 2009

NiO with novel flower-like morphology was prepared by using a two-step, template- and surfactant-free, environmentally friendly method. Flower-like NiO was composed of many irregular nanosheets that were assembled together by weak interactions. The as-prepared materials were characterized by X-ray diffraction, thermogravimetric analysis, differential scanning calorimetry, scanning electron microscopy, transmission electron microscopy with selected area electron diffraction patterns, N<sub>2</sub> sorption, temperature-programmed reduction with CO, X-ray photoelectron spectroscopy (XPS), and in situ Fourier transform infrared (FT-IR) for CO adsorption. The catalytic behaviors for CO oxidation were studied by using a fixed bed microreactor. Compared to NiO nanoparticles, we found the flower-like NiO possessed a larger surface area, bimodal pore size distribution, higher reducibility, and superior catalytic activity for CO oxidation. The XPS and CO in situ FT-IR results showed that its catalytic property was morphology dependent. The flower-like morphology provided more coordinate unsaturated Ni atoms, more oxygen vacancies, and more defect sites, which made the flower-like NiO have a strong interaction with CO and more active sites for catalytic reactions. Further studies showed that a mild condition for thermodecomposition of the precursor was necessary to preserve the flower-like morphology because of the large discrepancy of the crystalline cell structures between the  $\beta$ -Ni(OH)<sub>2</sub> precursor and product of NiO.

## Introduction

Materials in nanoscale have fascinated the scientific community in the recent years because of their unusual physical and chemical properties compared to those of their bulk counterparts. These materials have potential applications such as catalysts, drug delivery materials, photonic materials, and battery materials.<sup>1–4</sup> The morphology and size of the nanomaterial could greatly influence their optical, electronic, magnetic, and catalytic properties.<sup>5–8</sup> Much progress has been made on the size control and morphology control of nanomaterials. Various materials with sizes in the range of several nanometers to micrometers were synthesized,<sup>9–12</sup> and a variety of morphologies have also been fabricated such as nanotubules, nanowires, nanorings, ordered hexagonal mesostructures, nanorods, etc.<sup>13–17</sup> In the current stage, synthesis of large scale self-assembly of nanoscale building blocks into complex structures has been a research hotspot. It is expected that if the morphology and assembly mode of original building units could be controlled, those of their secondary architecture would be adjusted to meet different needs.<sup>18–21</sup> Therefore, the work on organization and design synthesis needs to be developed for more novel properties and applications of nanomaterials.

As a *p*-type wide band gap semiconductor, NiO is a very promising material and has attracted increasing attention because of its extensive important applications as catalysts,<sup>22</sup> electrode materials for lithium ion batteries and fuel cells,<sup>23</sup> electrochromic films,<sup>24</sup> electrochemical supercapacitors,<sup>25</sup> and magnetic materials.<sup>26</sup> To date, many efforts have been attempted to prepare NiO nanostructures. Zhou and co-workers<sup>27</sup> prepared porous NiO nanomaterials by using mesoporous silicas, SBA-15 and KIT-6, as hard templates. Zheng and co-workers<sup>28</sup> obtained porous NiO flowers via a hydrothermal approach, and nickel dimethylglyoximate was used as the precursor. NiO microspheres were prepared by a hydrothermal route in the presence of poly(ethylene glycol) 4-nonylphenyl 3-sulfoethyl ether potassium salt (PENS),<sup>29</sup> but these methods suffered from the complication of the synthesis process and time-consuming removal of the hard and soft templates or organic additives. Therefore, developing a facile and feasible method to prepare NiO complex structures is a great challenge to material scientists.

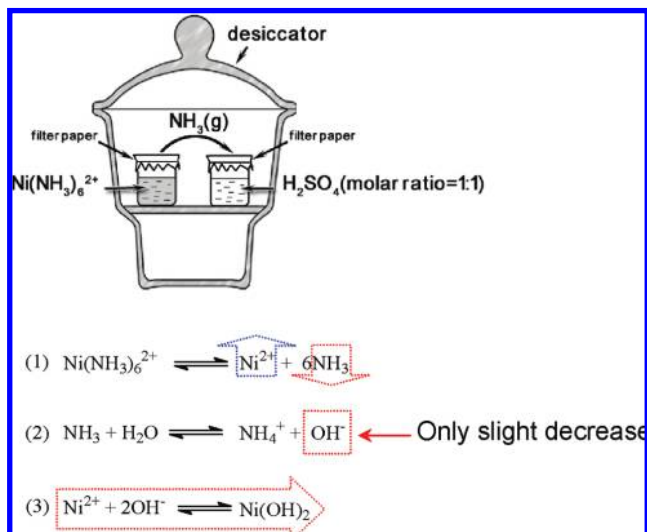
In this study, a convenient two-step route for fabricating NiO with flower-like morphology was developed without using hard or soft templates and other organic reagents. This method is environmentally friendly. The  $\beta$ -Ni(OH)<sub>2</sub> precursor was first prepared by an equilibria-shift route, and then the precursor was calcined to obtain flower-like NiO. Catalytic activity on CO oxidation of this NiO was superior to that of conventional nanoparticulate NiO. The differences for the catalytic properties of NiO with different morphologies in terms of reducibility, morphology, surface structure, and the ability of chemical adsorption were elucidated.

\* To whom correspondence should be addressed. (H.L. Chen) E-mail: hlchen@nju.edu.cn. Telephone: +86 25 83592369. Fax: +86 25 83597374. (Y.W. Chen) E-mail: ywchen@cc.ncu.edu.tw. Telephone: +886 3 4227151 extension 34203. Fax: +886 3 4252296.

<sup>†</sup> Key Laboratory of Mesoscopic Chemistry of MOE, Nanjing University.

<sup>‡</sup> The State Key Laboratory of Coordination Chemistry, Nanjing University.

<sup>§</sup> National Central University.

**SCHEME 1: Synthesis Procedure of the  $\beta$ -Ni(OH)<sub>2</sub> Precursor and Related Reaction Mechanism**

**Experimental Section**

**2.1. Synthesis Procedures.** All chemicals were used as received without further purification. In a typical experiment, 0.002 mol  $\text{Ni}(\text{CH}_3\text{COO})_2 \cdot 4\text{H}_2\text{O}$  was dissolved in 20.0 mL of deionized water in a 50 mL beaker.  $\text{NH}_3 \cdot \text{H}_2\text{O}$  (6 mol L<sup>-1</sup>) was added dropwise under magnetic stirring. A light green precipitate,  $\text{Ni}(\text{OH})_2$ , was formed.  $\text{NH}_3 \cdot \text{H}_2\text{O}$  was added continuously, and the precipitate was dissolved gradually. The color of the solution became darker, which indicated some of the  $\text{Ni}(\text{OH})_2$  was converted to the complex of  $\text{Ni}(\text{NH}_3)_6^{2+}$ . Finally, all of the precipitation dissolved, and the pH of the solution was about 10. The color of the solution turned dark blue [ $\text{Ni}(\text{NH}_3)_6^{2+}$ ]. Twenty milliliters of concentrated sulfuric acid was poured into another beaker. Both beakers were covered with filter paper and were placed in a desiccator. Precipitate with a light green color formed gradually. Twenty-four hours later, the product was separated by centrifugation, washed three times using deionized water, and then dried under vacuum at 40 °C. Finally, the precursor of  $\beta$ -Ni(OH)<sub>2</sub> was obtained. The synthesis procedure is illustrated in Scheme 1.

A determined amount of  $\beta$ -Ni(OH)<sub>2</sub> and  $\text{Ni}(\text{CH}_3\text{COO})_2 \cdot 4\text{H}_2\text{O}$  (for comparison) were put into crucibles. These two samples were calcined in a muffle furnace under a nitrogen atmosphere. The temperature ramp was 1 °C min<sup>-1</sup> from 20 to 400 °C, which was held for 1 h at 400 °C, so the materials in the crucible decomposed completely. It was then cooled naturally to room temperature. The NiO samples produced from  $\beta$ -Ni(OH)<sub>2</sub> and  $\text{Ni}(\text{CH}_3\text{COO})_2 \cdot 4\text{H}_2\text{O}$  were denoted as NiO-H (H for hydroxide) and NiO-A (A for acetate), respectively.

Another reference sample of NiO was obtained by calcination of  $\beta$ -Ni(OH)<sub>2</sub>. The temperature ramp was 15 °C min<sup>-1</sup>, and the duration time at 400 °C was prolonged to 2 h, while the other conditions were kept unchanged. This NiO sample was denoted as NiO-H15.

**2.2. Characterization.** X-ray diffraction patterns were obtained on a Shimadzu XD-3A diffractometer using Cu K $\alpha$  radiation ( $\lambda = 0.15406$  nm). The X-ray tube was operated under 35 kV and 15 mA. The scan speed was 4° min<sup>-1</sup>.

The morphology and particle size of  $\beta$ -Ni(OH)<sub>2</sub> and NiO were studied on a scan electron microscope (SEM, LEO 1530 VP) and transmission electron microscope (TEM, JEM-100CX) with selected area electron diffraction (SAED).

Nitrogen adsorption and desorption isotherms were measured at -196 °C using a Micromeritics ASAP 2020 system. The samples were degassed for 160 min at 300 °C in the degas port of the adsorption analyzer. Pore size distributions were calculated from the analysis of the desorption branch of the isotherm using the Barrett–Joyner–Halenda (BJH) algorithm. The specific surface areas of the samples were calculated following the multipoint BET (Brunauer–Emmett–Teller) procedure.

Thermogravimetric analysis (TGA) and differential scanning calorimetric (DSC) measurements were performed using a thermal analysis system (Model STA 409, Netzsch Geraetebau, Selb, Germany) and N<sub>2</sub> as carrier gas (100 mL min<sup>-1</sup>) at a heating rate of 10 °C min<sup>-1</sup> in a range of 30–500 °C.  $\alpha$ -Al<sub>2</sub>O<sub>3</sub> powder was used as reference.

CO-TPR (temperature-programmed reduction with CO) was carried out in a quartz U-tube reactor, and a 25 mg sample was used for each measurement. Prior to the reduction, the sample was pretreated in a N<sub>2</sub> stream at 100 °C for 1 h and then cooled to room temperature. After that, a CO–N<sub>2</sub> mixture (2% CO by volume) was switched on, and the temperature was increased linearly at a rate of 1 °C min<sup>-1</sup>. A thermal conductivity cell was used to detect the CO consumption in the reactant stream.

X-ray photoelectron spectra (XPS) were collected on an ESCALB MK-II spectrometer with nonmonochromatic Mg K $\alpha$  radiation ( $\lambda = 1253.6$  eV, 300W). During the data processing of the XPS spectra, binding energy values were calibrated by the C1s peak (284.6 eV) from the adventitious contamination layer. A Shirley-type background was subtracted from the signals, and the peaks were deconvoluted by Gaussian–Lorentz fitting using XPSPEAK software.

In situ FT-IR spectroscopy of adsorbed CO was carried out on a Nicolet 5700 FT-IR instrument running at 4 cm<sup>-1</sup> resolution. Self-supporting wafers of the NiO samples were placed inside a commercial controlled environment chamber (HTC-3). Before the measurements, samples were pretreated in a high-purity N<sub>2</sub> stream at 400 °C for 1 h. After cooling to room temperature, CO (10.1%) and He (balance) were introduced to the cell, the temperature was increased at a rate of 10 °C min<sup>-1</sup>, and the spectra were recorded from room temperature to 400 °C under a high-purity N<sub>2</sub> stream.

**2.3. Catalytic Activity Test.** The catalytic activities of NiO for a CO + O<sub>2</sub> reaction were performed under a steady-state condition, involving a feed stream with a fixed composition of CO 1.6%, O<sub>2</sub> 20.8%, and N<sub>2</sub> 77.6% by volume, where N<sub>2</sub> was used as diluent. A quartz tube was used as a reactor, and the requisite quantity of a NiO sample (25 mg for each test) was used. The sample was pretreated in a N<sub>2</sub> stream at 100 °C for 1 h and then heated to reaction temperature. After that, the mixed gases were switched on. The reaction was carried out with the same space velocity of 30000 mL g<sup>-1</sup> h<sup>-1</sup>. Two chromatogram columns and a thermal conduction detector (TCD) were used for the purpose of analyzing the products. Column A was packed with 13 $\times$  molecular sieve (30–60 mesh) for separating O<sub>2</sub>, N<sub>2</sub>, and CO, and column B was packed with Porapak Q for CO<sub>2</sub> detection.

**3. Results and Discussion**

**3.1. Mechanism for Synthesis of the Precursor.** There are several equilibria in the  $\text{Ni}(\text{NH}_3)_6^{2+}$  solution as shown in Scheme 1. In the beginning, the  $\text{Ni}(\text{NH}_3)_6^{2+}$  complex ions were very stable due to the relative high concentration of NH<sub>3</sub>. Because it was a closed system, NH<sub>3</sub> would volatile from the solution and be absorbed by sulfuric acid in the other beaker, so equilibrium 1 shifted to the right side and some of the complex ions were

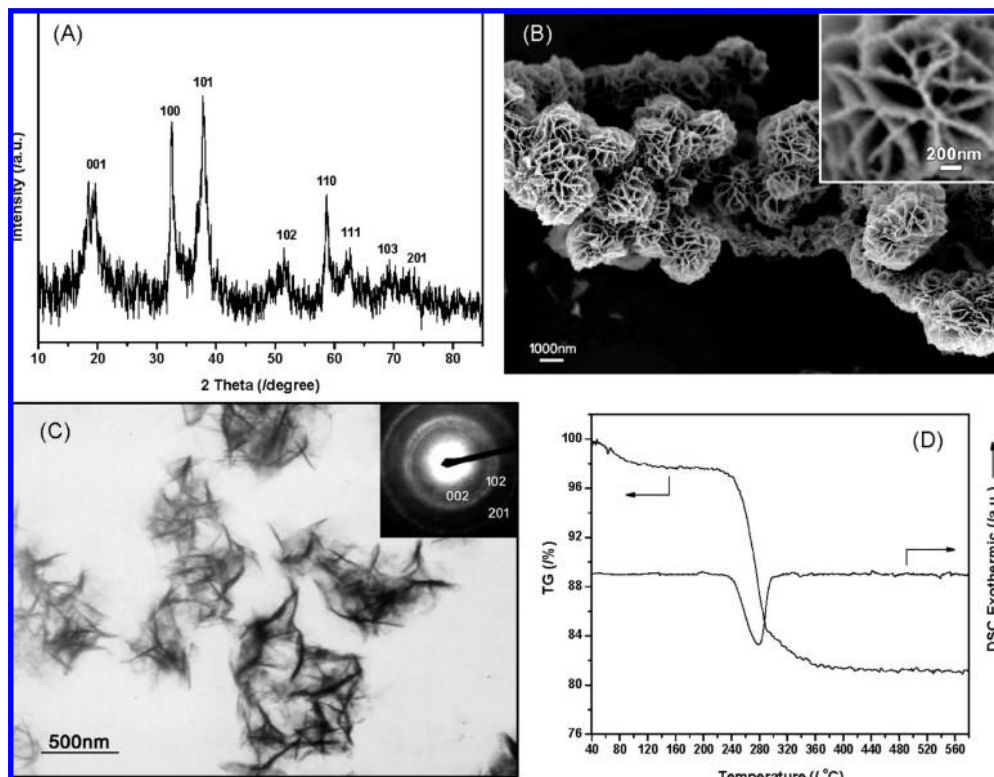


**Figure 1.** (A) XRD pattern, (B) SEM micrograph, (C) TEM micrograph, and (D) TGA-DSC curves of  $\beta$ -Ni(OH)<sub>2</sub> precursor. Inset in panel B is the SEM micrograph with high magnification. Inset in panel C is the SAED pattern of the precursor.

dissociated gradually, so the concentration of nickel ions increased. The concentration of NH<sub>3</sub> decreased due to the volatilization, and this would make equilibrium 2 shift to the left side. The equilibrium constant expressions for equilibrium 1 and 2 are

$$K_1 = \frac{[\text{Ni}^{2+}][\text{NH}_3]^6}{[\text{Ni}(\text{NH}_3)_6^{2+}]} \quad (1)$$

$$K_2 = \frac{[\text{NH}_4^+][\text{OH}^-]}{[\text{NH}_3]} \quad (2)$$

Because the power of NH<sub>3</sub> concentration in the expression of  $K_1$  is much higher than that of  $K_2$ , the concentration decrease is much more sensitive for equilibrium 1 than for equilibrium 2. Consequently, there is only a slight decrease of OH<sup>−</sup> concentration. On the basis of the overall consideration of the ion concentrations in the solution, the value of  $[\text{Ni}^{2+}][\text{OH}^-]^2$  would increase. When this concentration product was greater than the solubility product of nickel hydroxide under the experimental conditions, the precursor of  $\beta$ -Ni(OH)<sub>2</sub> was formed.

### 3.2. Morphology Study of Precursor and NiO Samples.

The XRD pattern of the precursor is shown in Figure 1A. All of the reflection peaks of the XRD pattern could be indexed to single phase  $\beta$ -Ni(OH)<sub>2</sub> with a crystalline hexagonal structure (JCPDS card 14-0117,  $a = 0.3126$  nm, and  $c = 0.4605$  nm). No impurity peaks are found, suggesting a high purity of the as-synthesized  $\beta$ -Ni(OH)<sub>2</sub>. The peaks are widened, and the intensities of the peaks are very weak, which implies that the crystalline structure of the precursor is not perfect and/or the crystalline size is very small. The average

crystalline size estimated by Sherrer's equation was only 5.98 nm [calculated by the most intense (101) diffraction peak].

The morphology of the precursor was investigated by SEM and TEM. The SEM micrograph in Figure 1B shows that the precursor consisted of a flower-like hierarchical structure, and the size was in the range between 2 and 3  $\mu\text{m}$ . The structure was comprised of densely packed irregular sheets, with a thickness of 30–100 nm, which were assembled together. Figure 1C shows the TEM micrograph of the precursor. The flower-like structure was destroyed by the ultrasonic treatment during the sample preparation before the TEM test, indicating that the interaction among sheets was not strong. The sheets presented a curved shape, and the thickness was 5–30 nm, which was less than the result obtained from SEM. The reason for this difference is because there are several layers of sheets assembled together in a SEM test. The selected area electron diffraction (SAED) of the precursor is shown in the inset of Figure 1C. The diffraction rings correspond to the diffractions of (002), (102), and (201) planes of  $\beta$ -Ni(OH)<sub>2</sub>, which proves the multicrystalline nature of the precursor. Furthermore, the diffraction rings were a little blurry, which indicated that the crystal structure of the precursor was not good enough. These results are consistent with the XRD results.

The TG-DSC results are shown in Figure 1D, and the total weight loss was about 19%, which was due to the decomposition of Ni(OH)<sub>2</sub> as in the following equation



The weight loss is consistent with the theoretical value (19.4%) calculated by this reaction. The result also indirectly proves that the precursor was Ni(OH)<sub>2</sub>. There is an endothermic peak in the DSC curve at about 284 °C, which is relatively lower than the value reported by Liang's group,<sup>30</sup> indicating



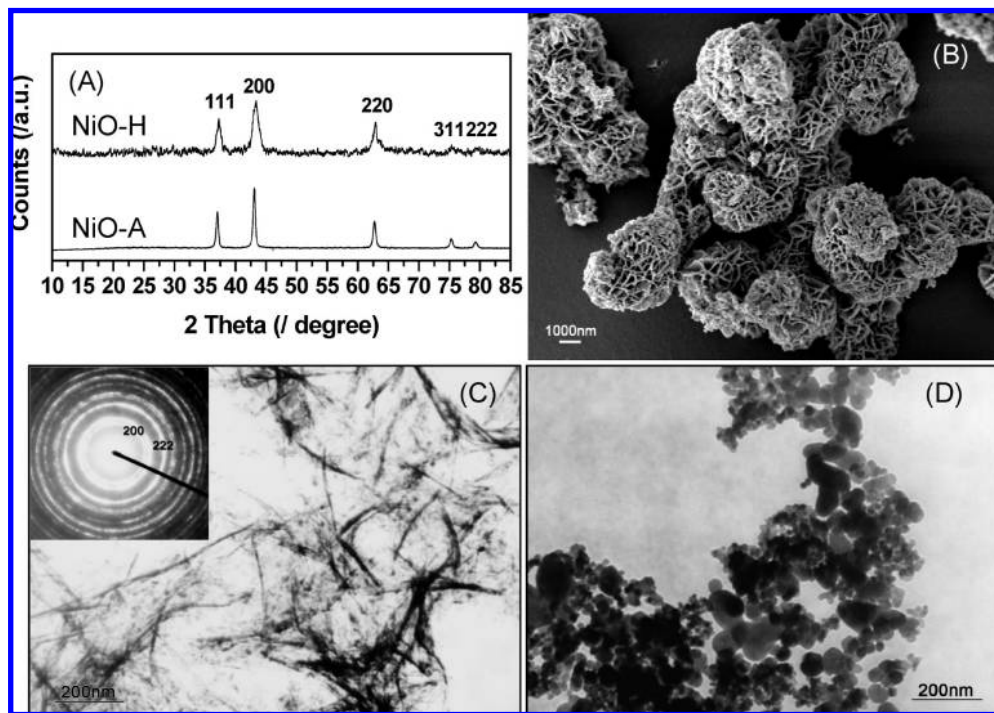


**Figure 2.** (A) XRD patterns of NiO-H and NiO-A. (B) SEM and (C) TEM micrographs of NiO-H. Inset in panel C is SAED pattern of NiO-H. (D) TEM micrograph of NiO-A.

**TABLE 1: Physical Properties of NiO-H and NiO-A**

sample	average crystallite size (nm)	specific surface area ( $\text{m}^2 \text{g}^{-1}$ )
NiO-H	8.45	88.8
NiO-A	20.11	42.1

that the precursor with flower-like morphology is more easily thermodecomposed. The pyrolysis of the precursor was complete before 400 °C, so 400 °C was chosen in this study as the decomposition temperature to obtain NiO.

The product of the thermodecomposition from the  $\beta$ -Ni(OH)<sub>2</sub> precursor (denoted as NiO-H) was studied by XRD, SEM, and TEM (with SAED). Figure 2A shows the XRD patterns of the products. All of the reflections could be indexed to the face-centered cubic (fcc) NiO phase. The positions of the corresponding peaks are in good agreement with the reported data (JCPDS card 71-1179,  $a = 0.41780 \text{ nm}$ ), and no peaks due to  $\beta$ -Ni(OH)<sub>2</sub> are observed by XRD. The XRD pattern of NiO decomposed from nickel acetate (denoted as NiO-A) is also shown in Figure 2A, and similar results are obtained as NiO-H, indicating the  $\beta$ -Ni(OH)<sub>2</sub> precursor and nickel acetate are decomposed completely to NiO under the experiment conditions. It is noticed that the corresponding peak width of NiO-H is larger than NiO-A. The average crystalline sizes of the two types of NiO were calculated by Sherrer's equation on the basis of the strongest (200) reflection, and the results is listed in Table 1. The average crystalline size of NiO-H is smaller than NiO-A.

Figure 2B shows the SEM micrograph of NiO-H, and it could be observed that the flower-like morphology of the precursor is preserved after the calcination process. A TEM photo of NiO-H is presented in Figure 2C, and the sheets structure is observed clearly. The SAED result in the inset of Figure 2C gives distinct diffraction rings corresponding to the (200) and (222) planes of NiO. The size of the sheet is about 6 to 10 nm. Figure 2D shows the TEM photo of the comparison sample of NiO-A, which is composed of nanoparticles. The sizes of the

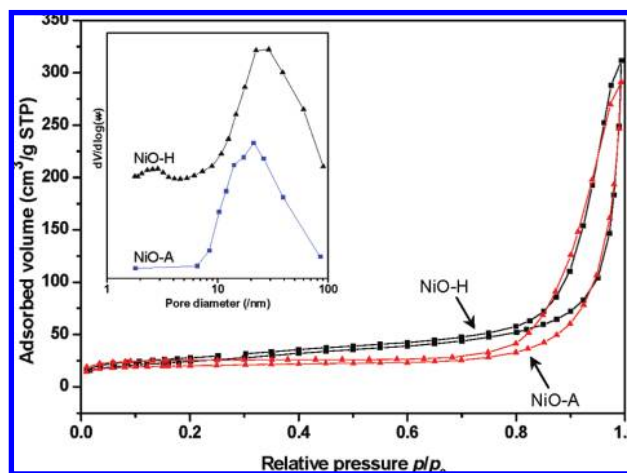


**Figure 3.** N<sub>2</sub> adsorption and desorption isotherms of NiO-H and NiO-A. Inset is the corresponding pore size distribution of NiO-H and NiO-A.

particles are mostly in the range of 10 nm to 60 nm. The results measured from TEM micrographs are different from the values from Sherrer's equation as shown in Table 1. Because the results by Sherrer's equation are average crystallite size and the morphologies of the two NiO samples are not uniform and the morphology of NiO-H is not spherical, the discrepancy is acceptable.

The texture properties were further elucidated by N<sub>2</sub> sorption analysis. The specific surface area of NiO-H was 88.8  $\text{m}^2 \text{g}^{-1}$ , and the surface area of NiO-A was only 42.1  $\text{m}^2 \text{g}^{-1}$ . Both NiO samples showed IUPAC type IV isotherms and H<sub>3</sub> type hysteresis. The hysteresis loops appeared nearly  $p/p_0 = 0.8$ , indicating that the pore size was relative large. This is confirmed by the pore size distribution curve (inset Figure 3). The pore sizes of these two types of NiO were in a very wide range, and the peaks of the curves were 26.1 nm for NiO-H and 20.5 nm for NiO-A. It is noticed that the pore size distribution curve of

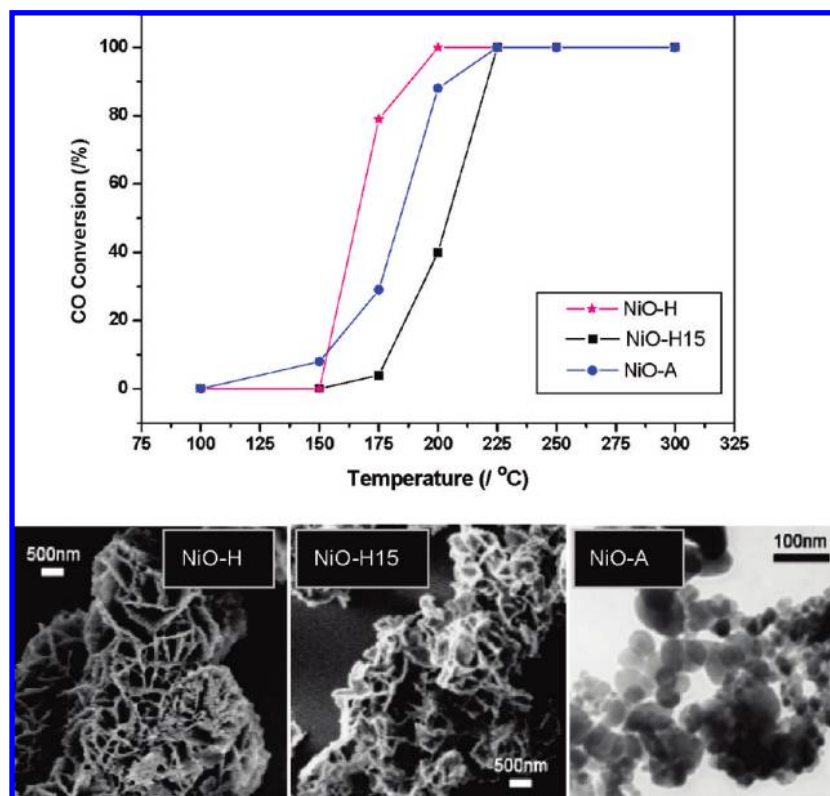


**Figure 4.** Catalytic activities of CO oxidation under different temperatures for NiO-H, NiO-H15, and NiO-A, and the corresponding morphologies of the samples.

NiO-H showed a small peak at 2.6 nm, indicating bimodal porosity in the mesoporous and macroporous regimes for NiO-H. This type of porosity would provide an efficient transport pathway for reactants to the interior of the NiO-H, which is beneficial for catalytic properties.

**3.3. Catalytic Properties.** Figure 4 shows the catalytic activities for CO oxidation over the NiO samples with different morphologies. The corresponding morphologies are also shown in Figure 4. The catalytic activity of NiO-H is superior to that for NiO-A. Further investigation proved that the catalytic property of NiO-H is morphology dependent. Another NiO sample (denoted as NiO-H15) is prepared by thermodecomposition of the  $\beta$ -Ni(OH)<sub>2</sub> precursor, and only the temperature ramp is changed to 15 °C min<sup>-1</sup>. The duration at 400 °C is prolonged to 2 h, and all other conditions are unchanged. The morphology of this sample is very different from that of NiO-H. The flower-like structure collapsed to a large extent, and the specific surface area of NiO-H15 was reduced to 40.0 m<sup>2</sup>·g<sup>-1</sup>. The catalytic activity also decreased dramatically. Although the BET surface area was close to NiO-A, the catalytic activity was much lower. The CO conversion at 175 °C for NiO-H was 88%, for NiO-A was 29%, and for NiO-H15 was only 4%. Generally, the catalysts at nanosize scale and with high surface area should provide the catalysts with higher activity.<sup>31,32</sup> However, surface area is not the only factor for determining the activity of the catalyst.<sup>33</sup> The NiO-H sample with flower-like morphology possessed more atoms on edges and corners than the NiO-A sample, which are the active sites for adsorption of reactants.<sup>33–35</sup> Once the flower-like morphology was damaged (like the situation for NiO-H15), the concentration of these active sites was reduced remarkably, so the activity of NiO-H15 decreased accordingly. The reason for the structure collapse of NiO-H15 was due to the great differences in crystalline structure between precursor  $\beta$ -Ni(OH)<sub>2</sub> (hexagonal,  $a = 0.3126$  nm,  $c = 0.4605$

nm) and NiO (cubic,  $a = 0.41780$  nm). During the conversion process of the precursor, the mild condition would help to eliminate the stress of the transformation in the structure, and the fast temperature increase would destroy the structure from the internal stress. Structure reformation and rearrangement of surface atoms would inevitable occur in the calcination process. These adjustments would make the surface trend more stable, so the number of coordinate unsaturated atoms and the atoms at edges and corners is decreased. Consequently, the CO adsorption ability reflected by the CO-FTIR was weakened, and the catalytic activity was decreased, apparently because the catalytic active sites (always with the coordinate unsaturated atoms) were reduced dramatically. Therefore, the surface atoms arrangement in NiO-H15 would differ largely from that of NiO-H. This difference in surface structure makes NiO-H15 have many dissimilar properties, which deeply influences its catalytic properties and CO adsorption capabilities. In summary, the catalytic activity of NiO is related to morphology, and the mild condition is necessary in the decomposition process to preserve the structure of the precursor.

The temperature-programmed reduction (TPR) technique has been extensively used to characterize the reducibility of the catalysts. The CO-TPR profiles of the NiO samples are shown in Figure 5A. In the region between 260 and 380 °C, there is only a single peak for each NiO sample. The peak temperature is in the order of NiO-H < NiO-H15 < NiO-A. The correlation of the activity and the peak temperature of CO-TPR are presented in Figure 5B. NiO-H shows the highest reducibility and the best catalytic properties. Generally, the catalyst with the lower reduction temperature always displays the higher catalytic properties, but it is not absolute for each instance. There is a different trend of NiO-H15. The TPR peak temperature of NiO-H15 was lower than that of NiO-A, but the catalytic activity of NiO-H15 was the lowest among three NiO samples. Because

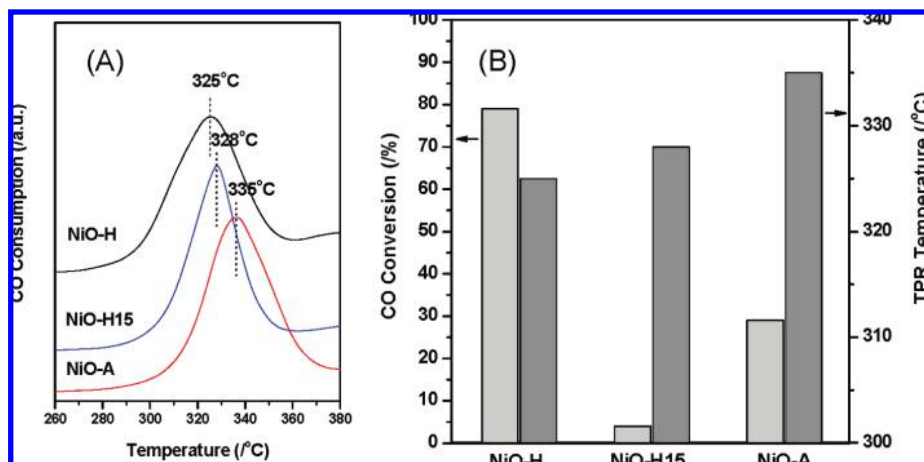


**Figure 5.** (A) CO-TPR profiles of NiO-H, NiO-H15, and NiO-A. (B) Relationship between the catalytic activities at 175 °C and the TPR peak temperature for NiO-H, NiO-H15, and NiO-A.

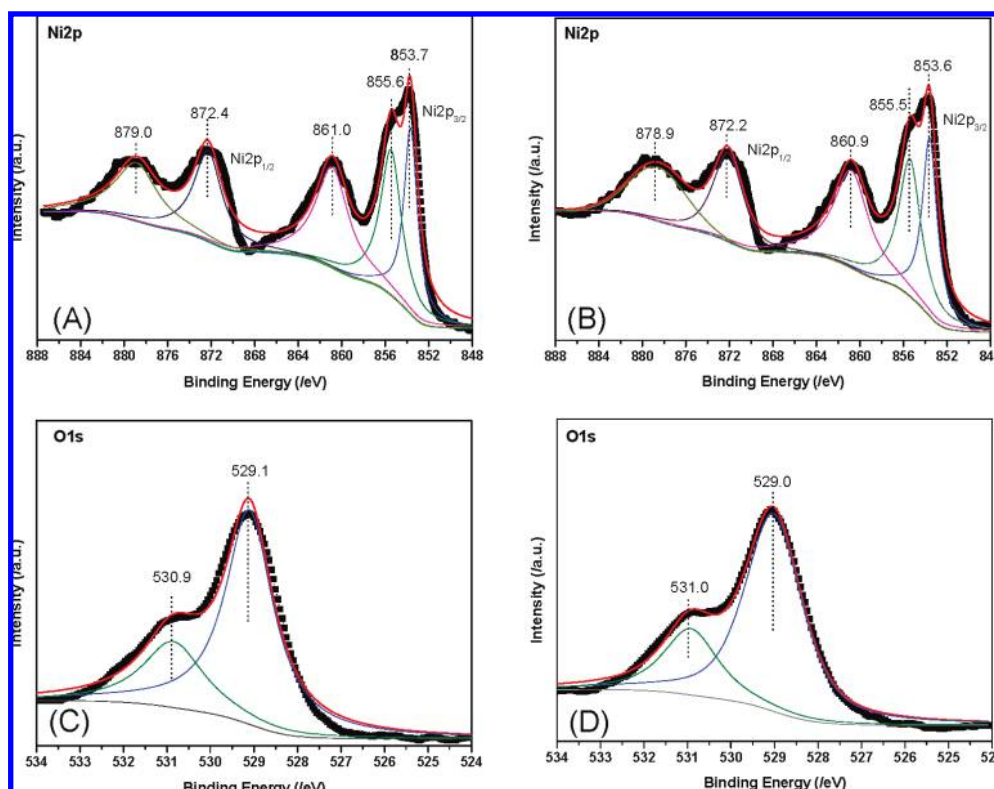


**Figure 6.** (A) and (C): Ni2p and O1s XPS spectra of NiO-H. (B) and (D): Ni2p and O1s XPS spectra of NiO-A.

the TPR test evaluates the bulk redox property of the catalyst and the catalytic reaction occurs on the surface of the catalyst, the catalytic activities are more sensitive to their surface structure. This kind of phenomena was also reported in Zhang's works.<sup>36</sup> They reported a kind of three-dimensionally ordered macroporous (3DOM) CuO–CeO<sub>2</sub> catalyst and studied the catalytic properties on the CO oxidation. They used particulate CuO–CeO<sub>2</sub> as a comparison. Although the TPR temperature of particulate CuO–CeO<sub>2</sub> is lower than the 3DOM CuO–CeO<sub>2</sub> and their BET surface areas are similar, the catalytic activity of 3DOM CuO–CeO<sub>2</sub> for CO oxidation is higher than the particulate sample.

Furthermore, the conversion of CO was 100% achieved for NiO-H, NiO-H15, and NiO-A when the temperature reached 225 °C, but from the TPR profiles, one could find that reduction of these samples did not occur until the temperature reached 260 °C. This means that the catalytic reaction progresses before

the bulk reduction take place. Therefore, the TPR results can only be used to evaluate the redox properties of the catalysts. The catalytic activities on CO oxidation are more sensitive to the surface structure as well as the morphology of the NiO samples.

**3.4. Surface Composition and Adsorption Properties.** To study the surface compositions and chemical states of the NiO samples, we conducted XPS studies, and the spectra are illustrated in Figure 6. Panels A and B of Figure 6 show the Ni2p core level signal of NiO-H and NiO-A, respectively. The Ni2p signal could be deconvoluted into five peaks. The binding energy at 853.7, 855.6, and 861.0 eV are attributed to the Ni2p<sub>3/2</sub> peaks, and the 872.4 and 879.0 eV peaks are attributed to Ni2p<sub>1/2</sub>. The positions of the peaks are almost the same for NiO-H and NiO-A within experimental error. The Ni2p<sub>3/2</sub> peaks are assigned to Ni(II) ions in the NiO samples, and the positions of the peaks are close to the value of pure



TABLE 2: XPS Results of NiO-H and NiO-A

sample	binding energy			area ratio (B.E. = 855.6 eV)/ total Ni2p <sub>3/2</sub> (%)	area ratio (B.E. = 531 eV)/ total O1s (%)	surface atom ratio (Ni:O)
	Ni2p <sub>3/2</sub> (eV)	Ni2p <sub>1/2</sub> (eV)	O1s (eV)			
NiO-H	853.7, 855.6	872.4	529.1	34.2	27.1	1.29
NiO-A	853.6, 855.5	872.2	529.0	33.5	21.9	1.23

NiO (854.2 eV) with a little shift to the lower binding energy. The main reason for this shift is due to the oxygen vacancy existing on the surface. The following results would prove this speculation. The peak at 855.6 eV is ambiguous. Tomellini<sup>37</sup> attributed this peak to Ni<sup>3+</sup> species on the NiO surface. Other researchers<sup>38,39</sup> reported that the intensity of this peak increased with the concentration of the defects. Soriano et al.<sup>40</sup> gave evidence based on the experimental results and theoretical calculation. They showed that the peak at 853.7 eV was due to NiO<sub>6</sub> in octahedral symmetry (bulk), and the peak at 855.6 eV was attributed to NiO<sub>5</sub> (or Ni<sup>2+</sup>, even with a lower coordinate number) in pyramidal symmetry. It was the surface effect causing the emergence of this so-called nonlocal satellite peak. For NiO-H and NiO-A samples, there are many Ni atoms on the surface because of the irregular morphology (for NiO-H) and nanosize nature (both for NiO-H and NiO-A). Many coordinate unsaturated atoms exist in these NiO samples. The ratio of the area of the peak at 855.6 eV versus the total area of the Ni2p<sub>3/2</sub> peaks would be an indication to some extent of the amount of Ni atoms in coordinate unsaturated sites. The results are listed in Table 2. The ratio for NiO-H (34.2%) was higher than that of NiO-A (33.5%), indicating that the flower-like morphology had more unsaturated Ni atoms. The O1s spectra of NiO-H and NiO-A are displayed in panels C and D of Figure 6, respectively. The O1s peaks are also deconvoluted, and there is a distinct peak at 529.1 eV and a shoulder peak at 530.9 eV. The shoulder peak has been proposed for the defect sites within the oxide crystal,<sup>41,42</sup> adsorbed oxygen,<sup>43</sup> or hydroxide species.<sup>44</sup> Here, we attribute the peak to the existence of defect sites on the NiO surface as shown in Table 2. The ratio of the peak at 530.9 eV versus the total O1s peaks for NiO-H was 27.1% for NiO-H and for NiO-A was only 21.9%, indicating that there were more surface defect sites on the NiO-H sample. The atomic ratio calculated by XPS results was 1.29 for NiO-H and 1.23 for NiO-A. The results show that there were more oxygen vacancies existing on the surface of NiO-H, and the lack of

highly electronegative oxygen atoms would lower the binding energy of Ni. This result is in good agreement with the Ni2p XPS results. More oxygen vacancies and more coordinate unsaturated sites existing on the surface of NiO-H gave NiO-H more intrinsic advantages in many aspects. These results could explain the easier reduction and higher activity of the NiO-H sample.

CO has been extensively used as a probe molecule in IR studies.<sup>45–47</sup> The investigations are conducted in this study using CO in situ FT-IR to study the chemical adsorption properties of NiO with different morphologies. The results are illustrated in Figure 7. Four bands at 2057, 2092, 2117, and 2175 cm<sup>-1</sup> are observed. The band at 2175 cm<sup>-1</sup> is ascribed to CO coordinated to Ni<sup>2+</sup> ions and forming a semilayer on the (100) faces of NiO crystallites. Two low-intensity bands, 2117 and 2092 cm<sup>-1</sup>, are attributed to Ni<sup>2+</sup>-CO or Ni<sup>2+</sup>(CO)<sub>2</sub> complexes, respectively. The band at 2057 cm<sup>-1</sup> is typical of carbonyls on metallic nickel, which is formed by the CO reduction of NiO under experimental conditions.<sup>48–54</sup> In particular, several studies described the interactions of CO with coordinate unsaturated Ni<sup>2+</sup> ions on the surface of vacuum-cleaved single-crystal oxides (or thin films grown on metal)<sup>55</sup> or on high surface area oxides.<sup>56</sup> It is widely accepted that CO binds to Ni<sup>2+</sup> ions by a  $\sigma$  bond with electrostatic interaction. Calculations have shown that the  $\pi$ -back-donation in the Ni<sup>2+</sup>-CO bond was negligible.<sup>57</sup> Generally, the Ni<sup>2+</sup>-CO species is easily decomposed upon evacuation at room temperature and is often observed at low temperature only. An exception is given with Ni<sup>2+</sup>-exchanged zeolites, where the carbonyls are stable at room temperature and disappear only upon outgassing at 100 °C.<sup>58,59</sup> In this case, the appearance of bands around 2220 cm<sup>-1</sup> has been explained by considering the combination of a high number of coordinative vacancies and the high electrophilicity of the cations, which implies that CO is strongly electrostatically bonded. Similar results are obtained for our NiO samples. The bands are also stable under room temperature and even under higher temperature for NiO-

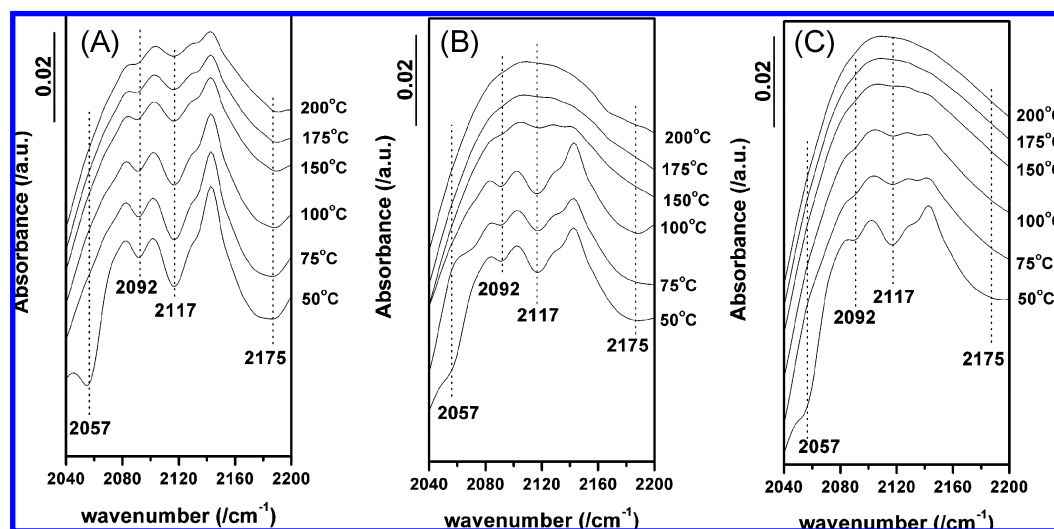


Figure 7. CO in situ FT-IR spectra under different temperatures: (A) NiO-H, (B) NiO-H15, and (C) NiO-A.



H. The stability is also due to the existence of abundant coordinate unsaturated sites existing on the samples. When the temperature is increased, these bands are reduced for all of the NiO samples, which suggest that the adsorption of CO is weakened. It is noticeable that the 2092, 2117, and 2175  $\text{cm}^{-1}$  bands for NiO-H could be identified until the temperature reached 150 °C. These bands nearly disappeared at 100 and 150 °C for the NiO-A and NiO-H15 samples, respectively. Considering the relatively low activities of the NiO samples under 150 °C, we find the intensity reduction for the carbonyl  $\text{Ni}^{2+}$  bands must be due to the desorption process of CO, which indicates that the adsorption ability of NiO-H is higher than that of the other two NiO samples. As one knows, it is a key step that the reactants should be adsorbed onto the surface of the catalysts so the subsequent steps can take place, and enough energy is needed to trigger the following reaction. If the adsorption strength is too weak, the reactants will desorb before the subsequent reactions take place, and consequently, the activity will be low. Surely the CO adsorption could not be too strong, otherwise, the active sites would be held by CO molecules, which would prevent the oxygen adsorption–dissociation process from taking place. Therefore, the “proper” strength of CO adsorption is favorable in the CO oxidation as in the instance of NiO-H. Because most surface coordinate unsaturated sites and most oxygen vacancies as well as structure defects exist on NiO-H, the NiO-H sample has the proper strength interaction with CO molecules that is favored for the CO oxidation reactions, so it has the highest activity. This is consistent with the XPS and CO TPR results.

## Conclusion

In summary, NiO with novel flower-like morphology was prepared via a two-step, template- and surfactant-free, environmentally friendly method. Flower-like NiO was composed of many irregular nanosheets that were assembled together by weak interactions. The flower-like morphology provides many special properties, including higher reducibility, larger specific surface area, and bimodal pore size distribution. The catalytic activity of the flower-like NiO on CO oxidation shows a morphology-dependent nature. The flower-like morphology gives more coordinate unsaturated Ni atoms, more oxygen vacancies, and more defect sites on the surface of NiO, which makes flower-like NiO have a strong interaction with CO. Because the crystalline structures between the  $\beta\text{-Ni}(\text{OH})_2$  precursor and NiO product were greatly different, mild conditions in thermodecomposition of the precursor are necessary to preserve the flower-like morphology.

**Acknowledgment.** This work was supported by the National Natural Science Foundation of China (50272029).

## References and Notes

- (1) Li, Z. Q.; Ding, Y.; Xiong, Y. J.; Yang, Q.; Xie, Y. *Chem. Commun.* **2005**, 918.
- (2) Dinsmore, A. D.; Hsu, M. F.; Nikolaides, M. G.; Marquez, M.; Bausch, A. R.; Weitz, D. A. *Science* **2002**, 298, 1006.
- (3) Zhong, Z. Y.; Yin, Y. D.; Gates, B.; Xia, Y. N. *Adv. Mater.* **2000**, 12, 206.
- (4) Lee, K. T.; Jung, Y. S.; Oh, S. M. *J. Am. Chem. Soc.* **2003**, 125, 5652.
- (5) Klimov, V. I. *Annu. Rev. Phys. Chem.* **2007**, 58, 635.
- (6) Li, L.; Hu, J.; Yang, W.; Alivisatos, A. P. *Nano Lett.* **2001**, 1, 349.
- (7) Kovtyukhova, N. I.; Mallouk, T. E. *Chem.—Eur. J.* **2002**, 8, 4354.
- (8) Zhu, J. X.; Gui, Z.; Ding, Y. Y.; Wang, Z. Z.; Hu, Y.; Zou, M. Q. *J. Phys. Chem. C* **2007**, 111, 5622.
- (9) Han, D. Y.; Yang, H. Y.; Shen, C. B.; Zhou, X.; Wang, F. H. *Powder Technol.* **2004**, 147, 113.
- (10) Lenggorgo, I. W.; Yoshifumi, I.; Noritaka, I.; Kikuo, O. *Mater. Res. Bull.* **2003**, 38, 1819.
- (11) Zhao, B.; Bao, J. H.; Chen, H. L. *Chin. J. Inorg. Chem.* **2006**, 56, 17.
- (12) Haruta, M. *Catal. Today* **1997**, 36, 153.
- (13) Liu, H. J.; Peng, T. Y.; Zhao, D. E.; Dai, K.; Peng, Z. H. *Mater. Chem. Phys.* **2004**, 87, 81.
- (14) Yang, O.; Sha, J.; Ma, X. Y.; Yang, D. R. *Mater. Lett.* **1967**, 59, 2005.
- (15) Liang, J. H.; Li, Y. D. *Chem. Lett.* **2003**, 32, 1126.
- (16) Sumit, B.; Ashwin, S.; Aruna, D.; Rao, P. M. *Langmuir* **2003**, 19, 5522.
- (17) Wang, W.; Liu, Y.; Xu, C.; Zheng, C.; Wang, G. *Chem. Phys. Lett.* **2002**, 362, 119.
- (18) Bitá, I.; Yang, J. K. W.; Jung, Y. S.; Ross, C. A.; Thomas, E. L.; Berggren, K. K. *Science* **2008**, 321, 939.
- (19) Cheng, J. J.; Mayes, A. M.; Ross, C. A. *Nat. Mater.* **2004**, 3, 823.
- (20) Cölfen, H.; Mann, S. *Angew. Chem., Int. Ed.* **2003**, 42, 2350.
- (21) Kanaras, A. G.; Sönnichsen, C.; Liu, H.; Alivisatos, A. P. *Nano Lett.* **2005**, 5, 2164.
- (22) Park, J.; Kang, E.; Son, S. U.; Park, H. M.; Lee, M. K.; Kim, J.; Kim, K. W.; Noh, H. J.; Park, J. H.; Bae, C. J.; Park, J. G.; Hyeon, T. *Adv. Mater.* **2005**, 17, 429.
- (23) Wang, X.; Li, L.; Zhang, Y. G.; Wang, S. T.; Zhang, Z. D.; Fei, L. F.; Qian, Y. T. *Cryst. Growth Des.* **2006**, 6, 2163.
- (24) Fantini, M. C. A.; Ferreira, F. F.; Gorenstein, A. *Solid State Ionics* **2002**, 152–153, 867.
- (25) Liu, K.; Anderson, M. J. *Electrochem. Soc.* **1996**, 143, 124.
- (26) Mattei, G.; Mazzoldi, P.; Post, M. L.; Buso, D.; Guglielmi, M.; Martucci, A. *Adv. Mater.* **2007**, 19, 561.
- (27) Yue, W. B.; Zhou, W. Z. *Chem. Mater.* **2007**, 19, 2359.
- (28) Ni, X. M.; Zhang, Y. F.; Tian, D. Y.; Zheng, H. G.; Wang, X. W. *J. Cryst. Growth* **2007**, 306, 418.
- (29) Kuang, D. B.; Lei, B. X.; Pan, Y. P.; Yu, X. Y.; Su, C. Y. *J. Phys. Chem. C* **2009**, 113, 5508.
- (30) Liang, Z. H.; Zhu, Y. J.; Hu, X. L. *J. Phys. Chem. B* **2004**, 108, 3488.
- (31) Ying, J. Y.; Mehnert, C. P.; Wong, M. S. *Angew. Chem., Int. Ed.* **1999**, 38, 56.
- (32) Boschloo, G.; Hagfeldt, A. *J. Phys. Chem. B* **2001**, 105, 3039.
- (33) Wang, D. S.; Xu, R.; Wang, X.; Li, Y. D. *Nanotechnology* **2006**, 17, 979.
- (34) Zhou, K. B.; Wang, X.; Sun, X. M.; Peng, Q.; Li, Y. D. *J. Catal.* **2005**, 229, 206.
- (35) Fuertes, A. B. *J. Phys. Chem. Solids* **2005**, 66, 741.
- (36) Zhang, Y.; Liang, H.; Gao, X. Y.; Liu, Y. *Catal. Commun.* **2009**, 10, 1432.
- (37) Tomellini, M. J. *J. Electron Spectrosc. Relat. Phenom.* **1992**, 58, 75.
- (38) Pacchioni, G. *Cluster Models for Surface and Bulk Phenomena*; Plenum Press: New York, 1992.
- (39) Sangaletti, L.; Depero, L. E.; Parmigiani, F. *Solid State Commun.* **1997**, 103, 421.
- (40) Soriano, L.; Preda, I.; Gutiérrez, A.; Palacín, S. *Phys. Rev. B: Condens. Matter Mater. Phys.* **2007**, 75, 233417.
- (41) Hagelin-Weaver, H. A. E.; Weaver, J. F.; Hoflund, G. B.; Salaita, G. N. *J. Electron Spectrosc. Relat. Phenom.* **2004**, 134, 139.
- (42) Norton, P. R.; Tapping, G. L.; Goodale, J. W. *Surf. Sci.* **1977**, 65, 13.
- (43) Benndorf, C.; Obl, C. N.; Thieme, F. *Surf. Sci.* **1982**, 121, 249.
- (44) Carley, A. F.; Rassias, S.; Roberts, M. W. *Surf. Sci.* **1983**, 135, 35.
- (45) Zecchina, A.; Scarano, D.; Bordiga, S.; Ricchiardi, G.; Spoto, G.; Geobaldo, F. *Catal. Today* **1996**, 27, 403.
- (46) Scarano, D.; Ricchiardi, G.; Bordiga, S.; Galletto, P.; Lamberti, C.; Spoto, G.; Zecchina, A. *Faraday Discuss.* **1996**, 119.
- (47) Zecchina, A.; Otero Are'án, C. *Chem. Soc. Rev.* **1996**, 25, 187.
- (48) Voroshilov, I.; Roev, L.; Kozub, G.; Rusov, M.; Lunev, N. *Kinet. Catal.* **1975**, 16, 1267.
- (49) Platero, E.; Coluccia, S.; Zecchina, A. *Surf. Sci.* **1986**, 171, 465.
- (50) Rodionova, T. A.; Tsyganenko, A. A.; Filimonov, V. N. *Adsorbts. Adsorbenty* **1982**, 10, 33.
- (51) Platero, E.; Scarano, D.; Spoto, G.; Zecchina, A. *Faraday Discuss. Chem. Soc.* **1985**, 80, 183.
- (52) Platero, E.; Coluccia, S.; Zecchina, A. *Langmuir* **1985**, 1, 407.
- (53) Courtois, M.; Teichner, S. J. *J. Catal.* **1962**, 1, 121.
- (54) Alexiev, A.; Terenin, A. *J. Catal.* **1965**, 4, 440.
- (55) Vesecky, S. M.; Xu, X. P.; Goodman, D. W. *J. Vac. Sci. Technol., A* **1994**, 12, 2114.
- (56) Zecchina, A.; Scarano, D.; Bordiga, S.; Spoto, G.; Lamberti, C. *Adv. Catal.* **2001**, 46, 265.
- (57) Neyman, K. M.; Rosch, N. *Chem. Phys.* **1993**, 177, 561.
- (58) Hadjiivanov, K.; Knozinger, H.; Mihaylov, M. *J. Phys. Chem. B* **2002**, 106, 2618.
- (59) Penkova, A.; Dzwigaj, S.; Kefirov, R.; Hadjiivanov, K.; Che, M. *J. Phys. Chem. C* **2007**, 111, 8623.